

# Seeing the Invisible: Machine learning-Based QPI Kernel Extraction via Latent Alignment

Yingshuai Ji<sup>\*†</sup>

ysji0505@gmail.com

Department of Computer Science and  
Engineering  
University of Notre Dame  
South Bend, IN, USA

Haomin Zhuang<sup>\*</sup>

hzhuang2@nd.edu

Department of Computer Science and  
Engineering  
University of Notre Dame  
South Bend, IN, USA

Matthew Toole

mtoole2@nd.edu

Department of Physics & Astronomy  
University of Notre Dame  
South Bend, IN, USA

James McKenzie

jmcken2@nd.edu

Department of Physics & Astronomy  
University of Notre Dame  
South Bend, IN, USA

Xiaolong Liu<sup>‡</sup>

xliu33@nd.edu

Department of Physics & Astronomy  
University of Notre Dame  
South Bend, IN, USA

Xiangliang Zhang<sup>‡</sup>

xzhang33@nd.edu

Department of Computer Science and  
Engineering  
University of Notre Dame  
South Bend, IN, USA

## ABSTRACT

Quasiparticle interference (QPI) imaging is a powerful tool for probing electronic structures in quantum materials, but extracting the single-scatterer QPI pattern (i.e., the *kernel*) from a multi-scatterer image remains a fundamentally ill-posed inverse problem. In this work, we propose the first AI-based framework for QPI kernel extraction. We introduce a two-step learning strategy that decouples kernel representation learning from observation-to-kernel inference. In the first step, we train a variational autoencoder to learn a compact latent space of scattering kernels. In the second step, we align the latent representation of QPI observations with those of the pre-learned kernels using a dedicated encoder. This design enables the model to infer kernels robustly even under complex, entangled scattering conditions. We construct a diverse and physically realistic QPI dataset comprising 100 unique kernels and evaluate our method against a direct one-step baseline. Experimental results demonstrate that our approach achieves significantly higher extraction accuracy, and improved generalization to unseen kernels.

## KEYWORDS

Machine Learning for Physics, Inverse Problems, Quasiparticle Interference (QPI), QPI Kernel Extraction, Variational Autoencoder

<sup>\*</sup>These authors contributed equally to this work.

<sup>†</sup>Work done via internship at the University of Notre Dame.

<sup>‡‡</sup>Corresponding authors.

Permission to make digital or hard copies of all or part of this work for personal or classroom use is granted without fee provided that copies are not made or distributed for profit or commercial advantage and that copies bear this notice and the full citation on the first page. Copyrights for components of this work owned by others than the author(s) must be honored. Abstracting with credit is permitted. To copy otherwise, or republish, to post on servers or to redistribute to lists, requires prior specific permission and/or a fee. Request permissions from [permissions@acm.org](mailto:permissions@acm.org).  
*Conference'17, July 2017, Washington, DC, USA*

© 2025 Copyright held by the owner/author(s). Publication rights licensed to ACM.  
ACM ISBN 978-x-xxxx-xxxx-x/YY/MM.. \$15.00  
<https://doi.org/10.1145/nnnnnnn.nnnnnnn>

## ACM Reference Format:

Yingshuai Ji<sup>\*†</sup>, Haomin Zhuang<sup>\*</sup>, Matthew Toole, James McKenzie, Xiaolong Liu<sup>‡</sup>, and Xiangliang Zhang<sup>‡</sup>. 2025. Seeing the Invisible: Machine learning-Based QPI Kernel Extraction via Latent Alignment. In *Proceedings of ACM Conference (Conference'17)*. ACM, New York, NY, USA, 5 pages. <https://doi.org/10.1145/nnnnnnn.nnnnnnn>

## 1 INTRODUCTION

Understanding the behavior of electrons in quantum materials is a central challenge in modern condensed matter physics, with far-reaching implications for the development of superconductors, and other next-generation electronic systems [5]. One powerful experimental technique used to probe the electronic properties of such materials is *quasiparticle interference* (QPI) imaging via scanning tunneling microscopy (STM), which captures quantum interference patterns that arise from electrons elastically scattering off impurities in a material (usually characterized as atomic defects) [3]. QPI kernels contain rich information about the material's electronic band structure, Fermi surface topology, and even superconducting pairing mechanisms [1, 11]. The core of QPI analysis is to identify the interference pattern, or **kernel**, associated with a **single scatterer**, as this pattern can be used to extract momentum-space electronic structure using a Fourier transform. However, experimentally, it is challenging or impossible to find such single isolated defects in a sufficiently large defect-free region, due to the ubiquitousness of surface defects. Scientists thus have to analyze **QPI images with multiple defects**, where each defect acts as a scatterer that contributes to the overall interference pattern. However, because of their random distribution, QPI phase incoherence among scatterers greatly reduces the overall signal-to-noise ratio (S/N) of a multi-scatterer QPI pattern [2]. A useful physical analogy is to imagine a random distribution of many identical stones being dropped into a pool of water, and using the resulting superposition of ripples to deduce the ripple pattern from a single stone. In our QPI kernel extraction problem, as illustrated in Fig. 1, the task is to **deconvolute and infer the kernel  $\mathcal{A}$  based on a multi-scatterer QPI image (observation)  $\mathcal{Y}$  and the known defect locations (activation map)  $\mathcal{M}$** .

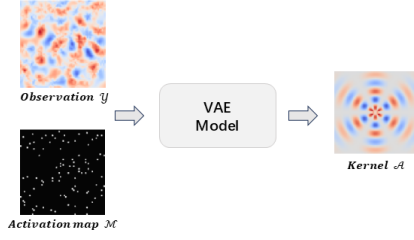


**Figure 1: Illustration of QPI Kernel Extraction Problem**

Existing solutions to this QPI kernel extraction problem are either zoom into each isolated defect in a small defect-free region [10], or try to extract a dispersion relation in a field of view with many defects directly [4]. Both approaches have disadvantages. For images taken in a small field of view, momentum space resolution is reduced. For images with many defects generating overlapping QPI patterns, the compromised S/N prevents the extraction of momentum space electronic structure with highest precision. This motivates our strategy of using **machine learning to analyze images of large regions with multiple defects and extract the kernel**.

We propose to leverage the power of convolutional neural networks (CNNs) to learn spatial patterns in the observed QPI signal and the expressive latent representations of a variational autoencoder (VAE) [6, 9] to infer the underlying scattering kernel. A straightforward solution is to design an encoder that jointly takes  $\mathcal{Y}$  and  $\mathcal{M}$  as input and directly decodes the scattering kernel  $\mathcal{A}$  using another decoder (as shown in Fig. 1). However, this direct approach suffers from poor performance due to the difficulty of learning a stable mapping from observations to kernels in a highly entangled space, as we demonstrate later in our evaluation results [7, 8].

To address these challenges, we propose a **two-step solution that decomposes the learning task into two more manageable subproblems**, as shown in Fig. 2 (Top). In the **first** step, we train a variational autoencoder where the scattering kernel  $\mathcal{A}$  is both the input and the target output. This step learns a **compact, semantically meaningful embedding space for kernels,  $\mathbf{h}_A$** . In the **second** step, we aim to **bridge the observation and kernel domains in their representation space**. Specifically, we train a separate encoder that maps the observed data ( $\mathcal{Y}, \mathcal{M}$ ) to a latent embedding  $\mathbf{h}_Y$ , which is then aligned with the latent representation ( $\mathbf{h}_A$ ) of the corresponding kernel produced by the step1-trained (and now frozen) encoder. By enforcing this alignment, the model learns to infer kernel representations from observations, enabling robust kernel extraction via the shared decoder (Fig. 2 Bottom).

We validate our two-step approach on simulated QPI datasets that cover a wide range of scattering environments and electronic structures, involving 100 distinct scattering kernels. These datasets are designed to reflect the diversity and complexity encountered in real QPI measurements, including variations in impurity configurations and band structures. Evaluation results demonstrate that our proposed method significantly outperforms the direct one-step baseline (e.g., Fig. 1) in terms of extraction accuracy, and generalization to unseen kernels. This can be better understood through analogy: the one-step solution is akin to recovering the ripple pattern of a single stone from a snapshot of overlapping waves, without first understanding the shape of individual ripples. Small shifts in stone

positions can drastically alter the observed interference, even if the ripple shape remains unchanged. Similarly, in QPI, the observed signal reflects entangled scattering effects, making direct inference unstable. Our two-step method addresses this by first learning the structure of individual kernels, then aligning observations within the same representation space to enable robust and generalizable extraction.

In summary, this work makes the following key contributions:

- We formulate QPI kernel extraction as a challenging inverse problem and propose the first machine learning-based solution to this task. Our principled two-step framework decouples kernel representation learning from observation-to-kernel inference, marking a step toward the broader integration of AI techniques into quantum materials research.
- We construct a diverse and physically realistic QPI dataset comprising 100 distinct scattering kernels across a variety of electronic structures and impurity configurations to support thorough quantitative evaluation. We will release the dataset to facilitate future research and benchmarking in machine learning for quantum materials.
- We demonstrate that our two-step method consistently outperforms the direct one-step baseline up to 23% of RMSE, presenting the first state-of-the-art AI-based solution to the QPI kernel extraction problem.

## 2 METHODOLOGY

To infer a kernel  $\mathcal{A}$  from the observed data, a pair consisting of an observation  $\mathcal{Y}$  and its corresponding activation map  $\mathcal{M}$ , we propose a two-step training strategy which results in encoder-decoder for inference shown in Fig. 2. In **Step 1**, a kernel VAE is trained to learn informative features from the kernels and accurately reconstruct them. Once training in Step 1 is complete, we freeze the kernel encoder and decoder. In **Step 2**, an **observation and activation map encoder** is trained to extract meaningful latent representations of the corresponding kernel, which should be aligned with the latent representations produced by the well-trained **kernel encoder** from Step 1 (i.e.,  $\mathbf{h}_Y$  and  $\mathbf{h}_A$  should be similar). During **inference**, a new observed data pair ( $\mathcal{Y}, \mathcal{M}$ ) is first processed by the **observation and activation map encoder** trained in Step 2. The resulting latent representations then pass through the **kernel decoder**, which comes from Step 1, to produce the final output, an image of the inferred kernel.

### 2.1 Kernel Encoder-Decoder

To learn effective latent representations for kernels, we train a **kernel encoder** mapping each kernel  $\mathcal{A}$  to a latent vector  $\mathbf{h}_A$ , which captures the underlying structure of the kernel. Subsequently, the **kernel decoder** reconstructs a kernel  $\hat{\mathcal{A}}$  from  $\mathbf{h}_A$ :

$$\mathbf{h}_A = \text{Encoder}_K(\mathcal{A}); \hat{\mathcal{A}} = \text{Decoder}_K(\mathbf{h}_A), \quad (1)$$

where the  $\text{Encoder}_K$  and  $\text{Decoder}_K$  represent the **kernel encoder** and the **kernel decoder** respectively.  $\text{Encoder}_K$  and  $\text{Decoder}_K$  are trained jointly by minimizing the difference between the reconstruction and the original kernel:

$$\mathcal{L}_{\text{MSE}} = \frac{1}{H \times L} \times \sqrt{\|\hat{\mathcal{A}} - \mathcal{A}\|^2}, \quad (2)$$

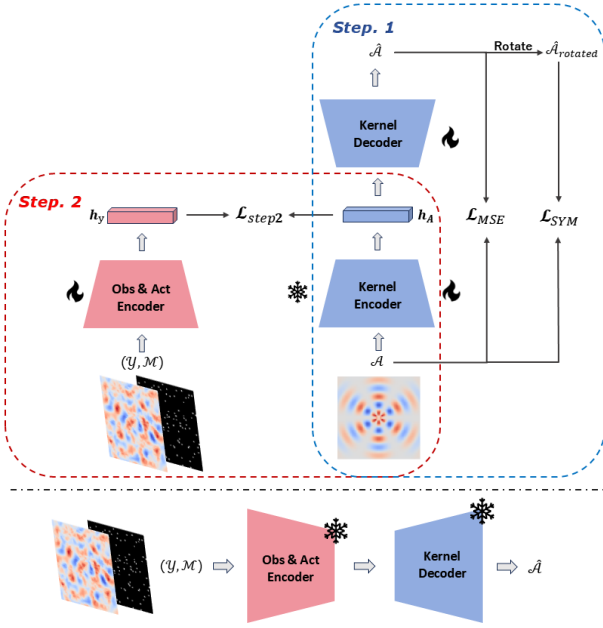


**Figure 2: Top: The proposed two-step training framework. Step 1 (blue box): training a VAE for kernel  $\mathcal{A}$  reconstruction using the losses  $\mathcal{L}_{MSE}$  and  $\mathcal{L}_{SYM}$ . Step 2 (red box): training the observation–activation encoder via aligning  $\mathbf{h}_A$  and  $\mathbf{h}_y$  (the kernel encoder is frozen). Bottom: The inference process.**

Where  $H$  and  $L$  are the height and width of the image respectively. Furthermore, taking account of the symmetrical characteristic that all kernels have, the ideal reconstruction should also be well-symmetric. Therefore, if the reconstruction is rotated by the angle between two axes of symmetry of the kernel, it should also be similar to the original one, for which a symmetric loss between the rotated reconstruction  $\hat{\mathcal{A}}_{rotated}$  and the kernel can be introduced:

$$\mathcal{L}_{SYM} = \frac{1}{H_r \times L_r} \times \sqrt{\|\hat{\mathcal{A}}_{rotated} - \mathcal{A}\|^2}, \quad (3)$$

Where  $H_r$  and  $L_r$  represents the height and width of the rotated image window respectively. Overall, the training objective of step 1 can be formalized as:

$$\mathcal{L}_{step1} = \mathcal{L}_{MSE} + \alpha \cdot \mathcal{L}_{SYM}, \quad (4)$$

where hyperparameter  $\alpha$  is the weight of  $\mathcal{L}_{SYM}$ . After training, the kernel encoder-decoder is frozen, of which the  $\text{Encoder}_K$  will serve as a reference for computing latent representations of kernels in Step 2, and the  $\text{Decoder}_K$  will be employed for inference.

## 2.2 Observation and Activation Map Encoder

In order to obtain the features for inferring the correct kernel from the observed data, another encoder is trained to align its output with the latent representation generated by  $\text{Encoder}_K$ . Therefore in Step 2, we train the **observation and activation map encoder** ( $\text{Encoder}_y$ ) to map each observed data pair  $(\mathcal{Y}, \mathcal{M})$  into the shared latent space of step1. To transform the observed data pair into a

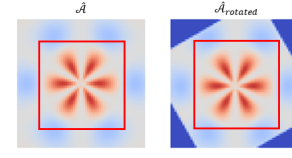


**Figure 3: Illustration of the symmetry loss  $\mathcal{L}_{SYM}$ : the reconstructed image is rotated by  $180^\circ$ ,  $120^\circ$ ,  $90^\circ$ , or  $60^\circ$  when there are 2-, 3-, 4-, or 6-fold symmetries, respectively. Only the values in the red box are taken into consideration.**

form acceptable to the encoder,  $\mathcal{Y}$  and  $\mathcal{M}$  are stacked as a two-channel input, and fed into the trainable encoder:

$$\mathbf{h}_y = \text{Encoder}_y(\mathcal{Y}, \mathcal{M}), \quad (5)$$

where  $\mathbf{h}_y$  is the output latent vector, and  $\text{Encoder}_y$  is implemented with the same structure as  $\text{Encoder}_K$ . To align the latent vector of observed data with that of the corresponding kernel, the  $\text{Encoder}_y$  is trained by minimizing the discrepancy loss between  $\mathbf{h}_y$  and  $\mathbf{h}_A$ :

$$\mathcal{L}_{step1} = \sqrt{\|\mathbf{h}_y - \mathbf{h}_A\|^2}, \quad (6)$$

where  $\mathbf{h}_A$  denotes the latent representations of the kernel  $\mathcal{A}$  corresponding to the observed data, which are obtained through the frozen  $\text{Encoder}_K$  trained in Step 1. This objective encourages the model to embed the observed QPI patterns into a latent space that is consistent with the kernel embeddings, thereby facilitating the learning of meaningful mappings from observed data to their underlying scattering kernels.

## 2.3 Inference Procedure

As shown in Fig. 2, the whole model is set frozen at the inference stage. Given a new input pair  $(\mathcal{Y}, \mathcal{M})$ ,  $\text{Encoder}_y$  trained in Step 2 is used to compute the predicted latent representations of the kernel, which is then passed to  $\text{Decoder}_K$  (trained in Step 1), to finally generate the inferred kernel image. Notably, the kernel encoder  $\text{Encoder}_K$  is not involved during inference, as it serves only as a reference during training in Step 2.

## 3 DATASET

**Dataset Overview.** In an experimental STM image, the QPI signal appears as oscillations centred at a scattering location and possesses either total, 2-, 3-, 4-, or 6-fold rotational symmetry, with material-specific properties determining the remaining details. Signals from each scatterer then interfere with one another throughout the image. To be more specific, the dataset consists of 100 uniquely kernels with 500 observations each for a total of 50,000 samples. Every sample has a real-space image of electronic structure (observation), a real-space image of the impurity configuration (activation map), and a real-space image of the corresponding scattering kernel. This dataset allows for the shape of the kernel to be seen clearly while maximizing efficiency of simulation.

**Dataset Construction.** The data are constructed through a phenomenological model (i.e. not physically exact) of each kernel that captures these properties. The general form of the kernel used in simulation is

$$\text{Kernel}(r, \theta) = \sin^2(A\theta + \varphi_1) \sin^2(Br + \varphi_2) e^{-cr^2} \quad (7)$$

where  $r$  is the distance from the defect location, and  $\theta$  is the angle with respect to the defect location. The free parameters are: 1)  $A$  selects the rotational symmetry (0 for total rotational symmetry,  $\{1, \frac{3}{2}, 2, 3\}$  for (2, 3, 4, 6)-fold respectively); 2)  $\varphi_1$  adjusts the orientation of the pattern ( $\varphi_1$  is  $\pi/2$  if  $A = 0$ ); 3)  $B$  is the frequency of the QPI pattern; 4)  $\varphi_2$  is the phase shift corresponding to the QPI oscillation; and 5)  $C$  is related to the decay length of the QPI pattern.

The constructed dataset consists of 100 unique kernels, where  $A$  is evenly distributed across each of the potential values, and  $\varphi_1, B, \varphi_2, C$  are randomly selected within physical reason. For each kernel, 500 images are generated, each of which has a random number of scattering centers (between 1–100) in randomly generated locations in the image, designed to represent a  $10 \times 10$  nm observation window with a resolution of  $64 \times 64$  pixels. The value for each pixel is determined by summing Eq. 7 across all defects present, superimposing the various single-defect patterns together.

## 4 EVALUATION EXPERIMENTS

**Training/Testing Splitting.** We adopt a structured data splitting strategy based on an 80/20 ratio for training and testing. First, the original kernel dataset—comprising individual kernel images—is divided into a kernel training set (80%) and a kernel testing set (20%). For the observation data ( $\mathcal{Y}$  and  $\mathcal{M}$ ), we construct two distinct test sets to evaluate the proposed method under both *In-Domain* and *Out-of-Domain* (OOD) generalization settings:

- **In-Domain (ID) Setting:** We take  $\mathcal{Y}$  and  $\mathcal{M}$  corresponding to kernels in the kernel training set and further split them into observed-data training and testing sets. This setting evaluates the model’s ability to infer seen kernels from unseen observation with unknown scattering centers.
- **Out-of-Domain (OOD) Setting:** We use  $\mathcal{Y}$  and  $\mathcal{M}$  associated with kernels in the kernel testing set to construct the OOD test set. This setup tests the model’s ability to generalize to entirely new kernels and their corresponding QPI patterns, which were not seen during training.

Using the earlier ripple analogy, the ID setting corresponds to inferring *which known stone caused new ripple patterns from different unknown positions or counts*. In contrast, OOD setting involves *inferring new, unseen types of stones*, each producing a different fundamental ripple.

**Evaluation Metrics and Baselines.** To quantitatively assess the quality of the inferred kernel images, we employ three widely-used regression metrics: Mean Absolute Error (MAE), Mean Squared Error (MSE), and Root Mean Squared Error (RMSE).

For evaluating the first ML solution for QPI Kernel Extraction, we compare the performance of two approaches:

- (1) **One-Step Baseline:** A single VAE is trained to directly map  $\mathcal{Y}$  and  $\mathcal{M}$  to  $\mathcal{A}$  (as shown in Fig. 1).
- (2) **Our Two-Step solution:** as introduced in Sec. 2.

**Implementation Details.** For both approaches, a pretrained VAE is employed, *madebyollin/sdxl-vae-fp16-fix* from AutoencoderKL in Hugging Face, with the following structure: A U-Net style network with 31 trainable layers (linear and convolutional) for the encoder, 51 trainable layers for the decoder, a  $4^*8^*8$  tensor as the latent space, and *SiLU* as the activation function. Training is conducted using *Adam*, learning rate of  $1e-4$ , batch size of 8, and for

**Table 1: Performance of our two-step approach and the one-step baseline on different settings. (best values in bold)**

Settings	Methods	MAE ↓	MSE ↓	RMSE ↓
ID	One-step Baseline	0.0213	0.0019	0.0340
	Two-step Approach	<b>0.0099</b>	<b>0.0003</b>	<b>0.0163</b>
OOD	One-step Baseline	0.0722	0.0216	0.1193
	Two-step Approach	<b>0.0595</b>	<b>0.0142</b>	<b>0.0924</b>

**Table 2: Ablation study about the symmetric loss**

Settings	Methods	MAE ↓	MSE ↓	RMSE ↓
OOD	w/ sym loss	<b>0.0595</b>	<b>0.0142</b>	<b>0.0924</b>
	w/o sym loss	0.0636	0.0179	0.1004

350 epochs at most in Step 1 and 40 epochs at most in Step 2. The hyperparameter  $\alpha$  in Eq. 4 is set 0.75.

### 4.1 Evaluation Results and Qualitative Analysis.

We evaluate both approaches under ID and OOD generalization settings. The results are reported in Table 1. In the **In-Domain** setting, both the one-step baseline and the proposed two-step method are capable of inferring kernel structures, reflecting the strong feature learning capacity of the variational autoencoder. However, the two-step method achieves significantly better inference quality. Specifically, it reduces the MAE from 0.0213 to 0.0099, MSE from 0.0019 to 0.0003, and RMSE from 0.0340 to 0.0163.

In the **Out-of-Domain** setting, the one-step method struggles to generalize, as it relies heavily on patterns learned from direct mappings between observation data and known kernels in the training set. Its performance deteriorates markedly, with MAE rising to 0.0722, MSE to 0.0216, and RMSE to 0.1193. Qualitative inspection confirms that many predicted kernels significantly deviate from the correct mode. In contrast, the two-step method maintains stronger generalization, reducing the OOD MAE to 0.0595, MSE to 0.0142, and RMSE to 0.0924—substantially outperforming the baseline. Fig. 4a confirms that our two-step method successfully captures an OOD kernel’s four-fold symmetry (see the extraction result of our method  $\mathcal{A}_{2-step}$  and the ground truth  $\mathcal{A}$ ), whereas the one-step baseline fails to infer this unseen structure ( $\mathcal{A}_{1-step}$ ).

We also analysis the latent space by conducting the t-SNE visualization, as shown in Fig. 5. Each cluster in the figure brings together the kernels with similar modes (simulation functions) of all possible folds. This indicates that the model distinguishes the kernels by mainly focusing on their modes, which means the model may have insufficient attention on the number of folds and inspires us a direction of the future work in Sec. 5.

**Ablation Study.** To verify the impact of symmetric loss  $\mathcal{L}_{SYM}$  (in Eq. 4), we conduct an ablation study, exploring the performances between w/ and w/o symmetric loss models, shown in Table 2. As we can see, there is a 8% improvement on RMSE when symmetric loss is added, showing the effectiveness of the symmetric loss. The example in Fig. 4b also confirms the better inferred kernel with the help of the symmetric loss.

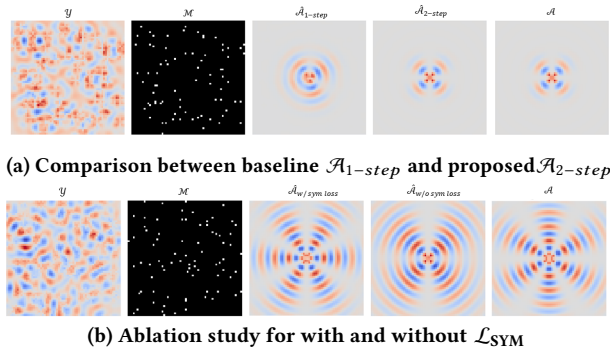


Figure 4: Case study examples

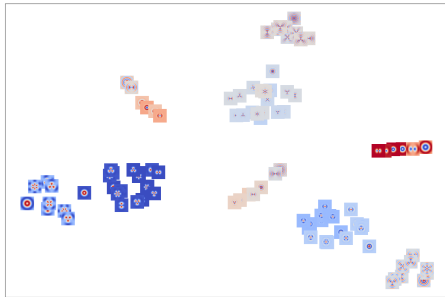


Figure 5: Visualization of kernel representation

## 5 CONCLUSION AND FUTURE WORK

In this paper, we propose a two-step training method based on variational autoencoder networks for the QPI kernel extraction problem. Specifically, in Step 1, we train a kernel encoder-decoder with a special loss function on kernel data to obtain effective latent representations. In Step 2, we introduce another encoder on observational data and train it by latent alignment. Lastly, we employ the encoder of Step 1 and the decoder of Step 2 in the inference task. Experiments in different settings confirm the effectiveness of our proposed method. In the future, as illustrated in Sec. 4, we will try to boost the model’s mastery of folds to generate inferences with correct numbers and further implement it in real-world circumstances.

## ACKNOWLEDGMENTS

This work is sponsored by the STIR program of University of Notre Dame.

## REFERENCES

- [1] Alexander V Balatsky, Ilya Vekhter, and Jian-Xin Zhu. 2006. Impurity-induced states in conventional and unconventional superconductors. *Reviews of Modern Physics* 78, 2 (2006), 373–433.
- [2] Sky C Cheung, John Y Shin, Yenson Lau, Zhengyu Chen, Ju Sun, Yuqian Zhang, Marvin A Müller, Ilya M Eremin, John N Wright, and Abhay N Pasupathy. 2020. Dictionary learning in Fourier-transform scanning tunneling spectroscopy. *Nature communications* 11, 1 (2020), 1081.
- [3] MF Crommie, Ch P Lutz, and DM Eigler. 1993. Imaging standing waves in a two-dimensional electron gas. *Nature* 363, 6429 (1993), 524–527.
- [4] JE Hoffman, K McElroy, D-H Lee, KM Lang, H Eisaki, S Uchida, and JC Davis. 2002. Imaging quasiparticle interference in Bi2Sr2CaCu2O8+  $\delta$ . *Science* 297, 5584 (2002), 1148–1151.
- [5] Bernhard Keimer and Joel E Moore. 2017. The physics of quantum materials. *Nature Physics* 13, 11 (2017), 1045–1055.

- [6] Diederik P Kingma and Max Welling. 2014. Auto-encoding variational bayes. In *Proceedings of the International Conference on Learning Representations (ICLR)*.
- [7] Diederik P Kingma and Max Welling. 2019. An introduction to variational autoencoders. *Foundations and Trends® in Machine Learning* 12, 4 (2019), 307–392.
- [8] Francesco Locatello, Stefan Bauer, Mario Lucic, Gunnar Raetsch, Sylvain Gelly, Bernhard Schölkopf, and Olivier Bachem. 2019. Challenging common assumptions in the unsupervised learning of disentangled representations. In *International Conference on Learning Representations (ICLR)*.
- [9] Danilo Jimenez Rezende, Shakir Mohamed, and Daan Wierstra. 2014. Stochastic backpropagation and approximate inference in deep generative models. In *International conference on machine learning*. PMLR, 1278–1286.
- [10] Rahul Sharma, Andreas Kreisel, Miguel Antonio Sulangi, Jakob Böker, Andrey Kostin, Milan P Allan, H Eisaki, Anna E Böhrer, Paul C Canfield, Ilya Eremin, et al. 2021. Multi-atom quasiparticle scattering interference for superconductor energy-gap symmetry determination. *npj Quantum Materials* 6, 1 (2021), 7.
- [11] François Vonau, Dominique Aubel, Gérard Gewinner, Stephan Zibrocki, Jean-Charles Peruchetti, Dominique Bolmont, and Laurent Simon. 2005. Evidence of Hole-Electron Quasiparticle Interference in ErSi 2 Semimetal. *Physical review letters* 95, 17 (2005), 176803.